The consistent in-situ global gridded temperature and salinity dataset, CORA OA 1960-2024

Tanguy Szekely[1] and Jean-Renaud Miadana[1]

[1]Société coopérative ARL OceanScope, 38 rue Jim Sevellec, 29200, Brest

Correspondence: Tanguy Szekely (tanguy.szekely@ocean-scope.com)

Abstract.

Gridded ocean products play a pivotal role in oceanographic and climate research, providing a framework for the cross-validation and calibration of satellite observations and in-situ data. This paper describes the latest evolution of the global gridded ocean objective analysis fields for temperature and salinity, distributed by the Copernicus Marine Service. It accounts for the update of the objective analysis first guess using monthly fields derived from the temporal interpolation of World Ocean Atlas 2023 (WOA23) decadal temperature and salinity climatologies. The new product provides monthly objective analysis fields for temperature and salinity with a 0.5° horizontal resolution and 186 vertical levels covering depths from 0 to 5500 m. The dataset is updated annually and covers the period from 1960 to December of the last complete year; the version described here covers 1960–2024. A full reprocessing is conducted every November, while an interim update covering the first six months of the current year is released each June. This product was compared with other reference 3D temperature and salinity datasets, as well as SST and SSS products. It exhibits strong consistency with all reference data, particularly over the 1985–2024 period. Notably, the effects of the Argo "fast salty drift" detected in other datasets after 2016, are limited in this product. The gridded product is freely accessible on the Copernicus Marine data store (https://data.marine.copernicus.eu/) under the ID INSITU_GLO_PHY_TS_OA_MY_013_052.

1 Introduction

According to IPCC (2023), the global ocean has warmed and the salinity changes observed since the mid-20th century are predominantly driven by anthropogenic forcing. To investigate these processes, the scientific community has developed an extensive suite of instruments for measuring ocean temperature and salinity. International initiatives were subsequently established to coordinate basin-scale measurement campaigns (Chapman, 1998; Bourlès et al., 2008; Teng et al., 2008) and to implement sustained observation systems such as the Global Drifter Program (Niiler, 2001). This international cooperation culminated in the late 1990s with the development of the Argo program (Roemmich et al., 2009; Jayne et al., 2017), which achieved near-global coverage to 2000 m by 2008 and extended observations to depths exceeding 5500 m by 2016.

The Coriolis Ocean dataset for ReAnalysis (CORA) was initiated by the French Coriolis project in 2008, incorporated into the European MyOcean project in 2010 (Bahurel et al., 2010; Cabanes et al., 2013), and subsequently integrated into the Copernicus Marine Service (Le Traon et al., 2019). It is provided as a delayed-mode, quality-controlled global in situ temperature and

salinity dataset, with the objective of delivering a high-quality record that includes carefully assigned quality flags and adjusted parameter values when available. CORA has been widely employed, particularly for ocean reanalysis applications (Lellouche et al., 2021), as well as for global ocean heat content assessments (von Schuckmann and Le Traon, 2011; von Schuckmann et al., 2013, 2023).

Since 2010, the CORA in situ dataset has been complemented by an objective analysis designed to provide a smooth three-dimensional representation of the monthly ocean temperature and salinity fields derived from it. This analysis has been yearly to twice yearly updated and extended using successive versions of the ISAS tool (Gaillard et al., 2009; Gaillard, 2012; Gaillard et al., 2016), and in its most recent release covers the period from the 1960s to the present.

The present article introduces the latest version of the CORA objective analysis product, which is distributed through the Copernicus Marine Service (https://doi.org/10.48670/mds-00383). Section 2 describes the data sources used to produce the objective analysis. The processing steps, methodology, and parameter settings are presented in Section 3. The resulting product is evaluated against comparable datasets in Section 4. Finally, conclusions and perspectives for future developments are provided in Section 5.

2 Data

2.1 Data source

This product is based on the temperature and salinity profiles extracted from the INSITU_GLO_PHY_TS_DISCRETE_MY_013_001 product , distributed by the Copernicus Marine Service (CMEMS, 2025). It is itself derived from the Copernicus Marine Service near–real-time (MYNRT) global in situ product INSITU_GLO_PHYBGCWAV_DISCRETE_MYNRT_013_030 (doi :https://doi.org/10.48670/moi-00036, extraction date : 03-02-2025). The product documentation gives the detail of the data sources (Copernicus Marine In Situ TAC partners, 2025, Table 5), and the near real time validation performed on the temperature and salinity profiles (Wehde et al., 2025). An additional delayed-mode validation has been performed using the methods described in Szekely et al. (2019), Gourrion et al. (2020), and Szekely (2024b). The delayed-mode validation relies on a set of tests, the most important of which is the MinMax test (Gourrion et al., 2020). This test flags the profiles whose values fall outside a reference range, computed for each 120 km wide grid cell from the extreme values of all the profiles of the previous CORA version. Each profile detected by this test is then visually checked by an operator, who decides whether the quality flags of its measurements must be changed. Pressure and depth are also checked by automatic tests: monotonicity of the pressure or depth axis and a range test. In the MYNRT and CORA datasets, flags 1 and 2 denote *good* and *probably good* data, while flags 3 and 4 denote *probably bad data that are potentially adjustable* and *bad* data. Only measurements flagged 1 or 2 after the delayed-mode validation, for both the parameter and the pressure or depth, are used in the present analysis. The full list of validation tests is given in Szekely (2025). The corrections applied to the profiles are listed in Table 1. For all profiles distributed in the CORA dataset, the adjusted version of a parameter, when available, is always used instead of its original value. These corrections concerns XBTs, Argo float and sea mammals. No corrections are applied to MBT, CTD or bottles profiles. The final dataset provides complete collection of profiles from 1950 to 2024. Additionally, it benefits from the synchronization of

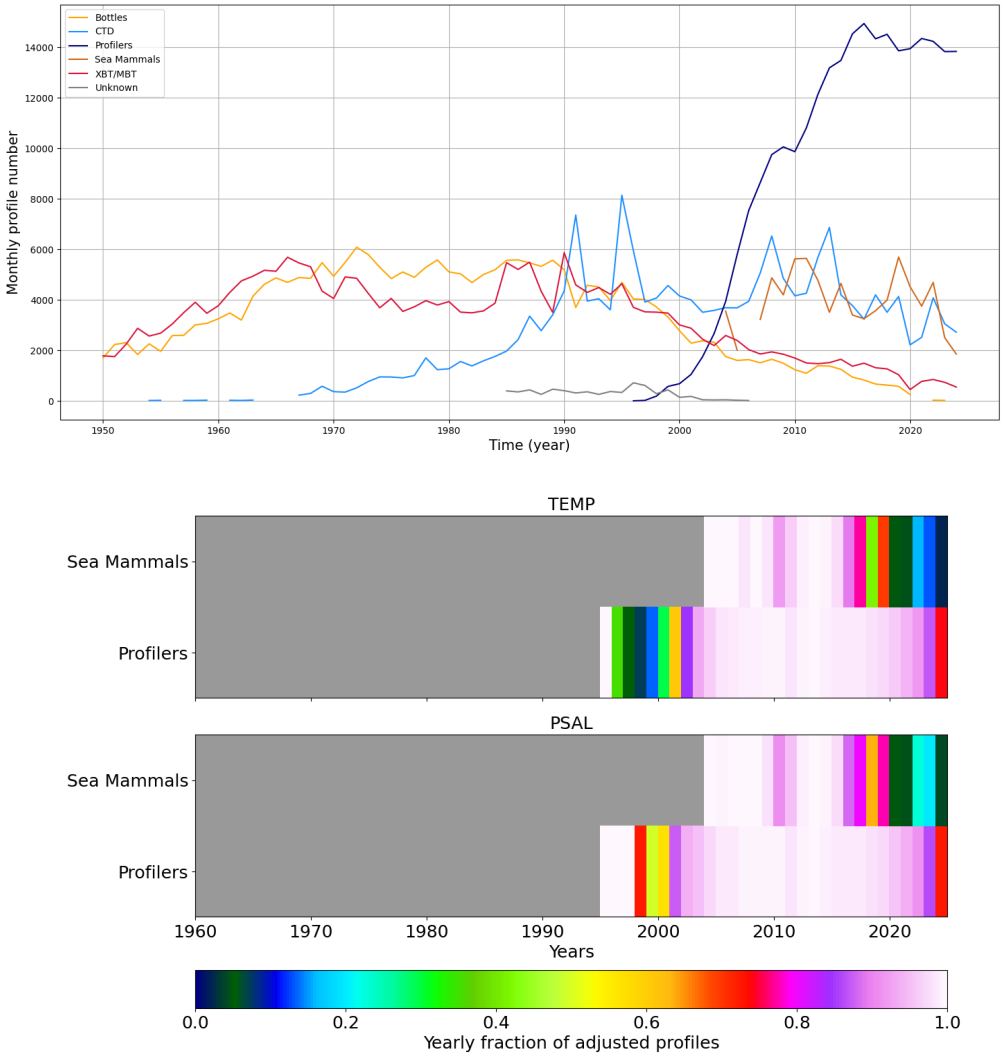


Figure 1. **Top** : Number of profiles distributed in `INSITU_GLO_PHY_TS_DISCRETE_MY_013_001` as a function of instrument type. Only profiles from the 1960–2024 period are used for the objective analysis. **Bot.** : fraction of adjusted profiles for sea mammals and profilers.

the Copernicus Marine MYNRT dataset with major data providers (World Ocean Database, Argo, etc.), ensuring that the best
60 available version of each profile remains with adjustments made by the original providers.

Figures 1, 2, and 4 provide insights into the data availability for the various data types used to produce the objective analysis. The yearly fraction of adjusted profiles is shown for profiling floats and sea mammals, because the Argo and MEOP (Marine Mammals Exploring the Oceans Pole to Pole) programs provide adjusted versions of their profiles. The "Bottles" category consists of measurements obtained by directly sampling seawater using bottles deployed along a cable. Since there are only

a limited number of bottles on each cable, most bottle profiles contain relatively few measurements, often taken at standard depths (see Fig. 2, top right panel). On the other hand, bottle profiles have made it possible to reach depths below 5500 m as early as the 1950s. The decrease in the yearly number of bottle data collected during the 2000s is mainly due to the difficulty of measurement. Most recent sampling is carried out with Rosette systems, which often group 10 to 20 bottles and can collect seawater at many vertical levels. However, the Rosette is heavy and must be deployed on a steel cable with a winch. Collecting samples from deep water therefore requires an oceanographic vessel equipped with a crane, and a single profile can take several hours to complete.

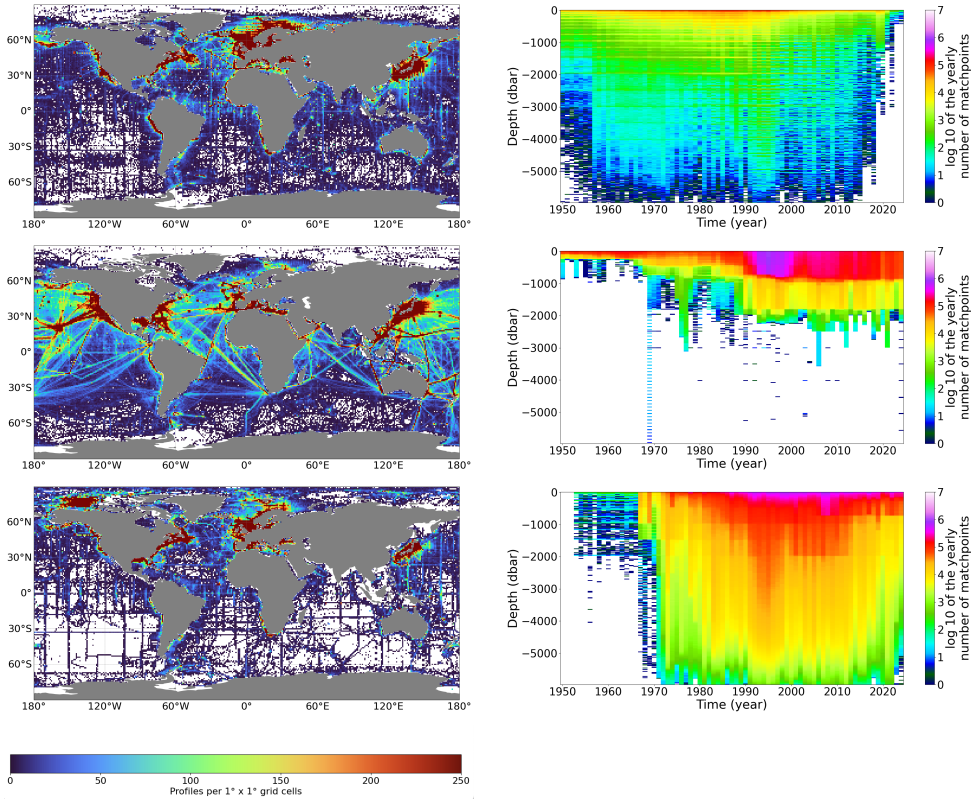


Figure 2. Left: Number of in-situ casts in 1-degree square grid cells from 1950 to 2024. **Right**: Yearly number of measurements in 20-meter vertical depth bins from 1950 to 2024. **Top** : Bottles casts. **Mid.** : XBT/MBT casts. **Bot.** : CTD casts.

The XBT and MBT instruments are bathythermographs deployed either along a cable (MBT) or as free-falling expendable probes (XBT) to measure ocean temperature. XBT casts can reach only a limited set of maximum depths, which appear as steps in the number of available data points in Fig. 2 (middle right). The depth of XBT measurements is estimated from the instrument's fall rate, a process that is susceptible to measurement errors. In the CORA dataset, XBT profiles are adjusted using the correction scheme of Cheng et al. (2014). This scheme determines fall-rate and offset correction coefficients by comparing co-located CTD and XBT profiles. The calculated coefficients vary with both the year and the probe type. The correction there-

Data type	Adjustment / bias correction	Applied by	Reference
Argo floats	Delayed-mode adjustments of pressure and salinity	Argo DACs	Wong et al. (2023)
Animal-mounted CTD	Adjusted temperature and salinity for MEOP profiles (2004–2017, release 2017-11); other profiles not adjusted	MEOP	Roquet et al. (2017)
XBT	Fall-rate and temperature offset correction, depending on year and probe type; HC test casts excluded from the analysis	CORA: Szekely (2025)	Cheng et al. (2014)
CTD, bottles, MBT	No adjustment	–	–

Table 1. Adjustments and bias corrections applied to the input profiles.

fore cannot be applied to the 375500 XBT profiles whose probe type is unknown or ambiguous, i.e. 37 % of the XBT profiles (Fig. 3), mostly between 1980 and 2005. Because these uncorrected profiles may introduce systematic temperature biases in the objective analysis, they are excluded from it. A dedicated analysis of these profiles, aiming to infer their probe type so that they can be corrected and reintegrated into the objective analysis, is planned for future versions of the product. They are not shown in Figure 2 (middle). Contrary to CTD casts, XBTs can be deployed from moving ships. As a result, Figure 2 (middle left) shows a higher density of profiles along the main shipping routes.

CTDs (Figure 2, bot.) are conductivity-temperature-depth casts, where salinity is derived from conductivity and temperature measurements. They are mostly deployed along cables from oceanographic ships, providing high vertical resolution profiles (often with more than one data point per dbar). The towed undulating CTD profiles available in the dataset from the 2000s are also classified as CTDs in this index. Like bottle casts, most CTDs are deployed from oceanographic ships at station and require several hours to complete. As a result, the number of CTD casts is lower in the Southern Ocean, leaving large areas uncovered.

The animal-mounted profiles (Fig. 4, top) come from CTD-like sensors deployed mostly on marine mammals and sea turtles. These instruments measure temperature and salinity along the animals' dives and often transmit low-resolution profiles when the animal surfaces to breathe. After a few months, if the instruments are retrieved, they provide access to the full high-resolution data. Major deployment sites include the Kerguelen Islands, the west coast of North America, the Labrador Sea, and Greenland, i.e. mostly high latitude areas. These deployments have yielded valuable observations along the seasonal migration routes of marine mammals, particularly in the Southern Ocean. Most profiles extend through the upper 1000 m of the ocean, with fewer reaching depths of up to 2000 m. The MYNRT dataset gathers both adjusted profiles extracted from the MEOP database (Roquet et al., 2017) and profiles originating from other sources (near-real-time versions of profiles, independent programs, etc.). All of these profiles are validated through the same procedures described above to ensure the homogeneity of

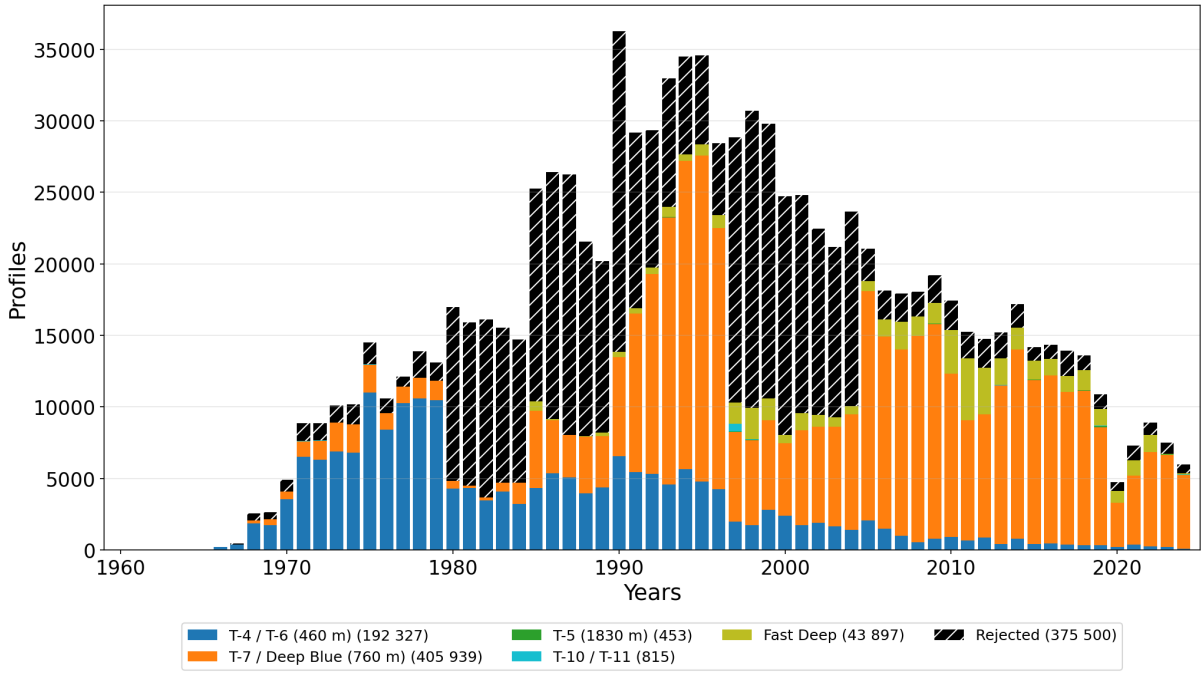


Figure 3. Yearly number of XBT profiles in the CORA dataset (November 2025 release), by probe type. The terminal depth of each probe type is given in parentheses, followed by the total number of profiles. Hatched bars: profiles with unknown or ambiguous probe type, which are not corrected and are excluded from the objective analysis.

the final dataset, even though the prevalence of errors is markedly lower among MEOP-sourced profiles than among other near-real-time profiles. As shown in Fig. 1, the MEOP program provides adjusted versions of the profiles over the period 2004-2017.

Argo profiles have been the most important deep-ocean observing system since the 2000s, providing near-global coverage with high data availability. The project was conceived in 1998 with the goal of deploying a network of autonomous profiling floats drifting freely at depth. These profilers have been deployed continuously since then, with a target of more than 3000 permanently operational floats covering the global ocean between 60°N and 60°S. The large-scale deployment of Deep Argo floats in 2015–2016 has further strengthened the vertical coverage, as these instruments can reach depths of 6000 m compared to 2000 m for the historical floats, as shown by the deepening of the data coverage in Figure 4 (middle right). The Argo processing framework provides an adjusted version for almost all of the profiles (see figure 1, Bot.)

The last data type shown in Fig. 4 corresponds to casts of unknown origin. The step increase in the number of available measurements at 1000 m between 1990 and 2010 (Fig. 4, bottom right), together with the profile distribution along the main shipping routes (Fig. 4, bottom left), suggests that many of these casts are in fact XBT profiles. Historical data were first only integrated in mid latitude, which explain the sharp decrease in the number of unknown casts north of 30°N and south of 35°S.

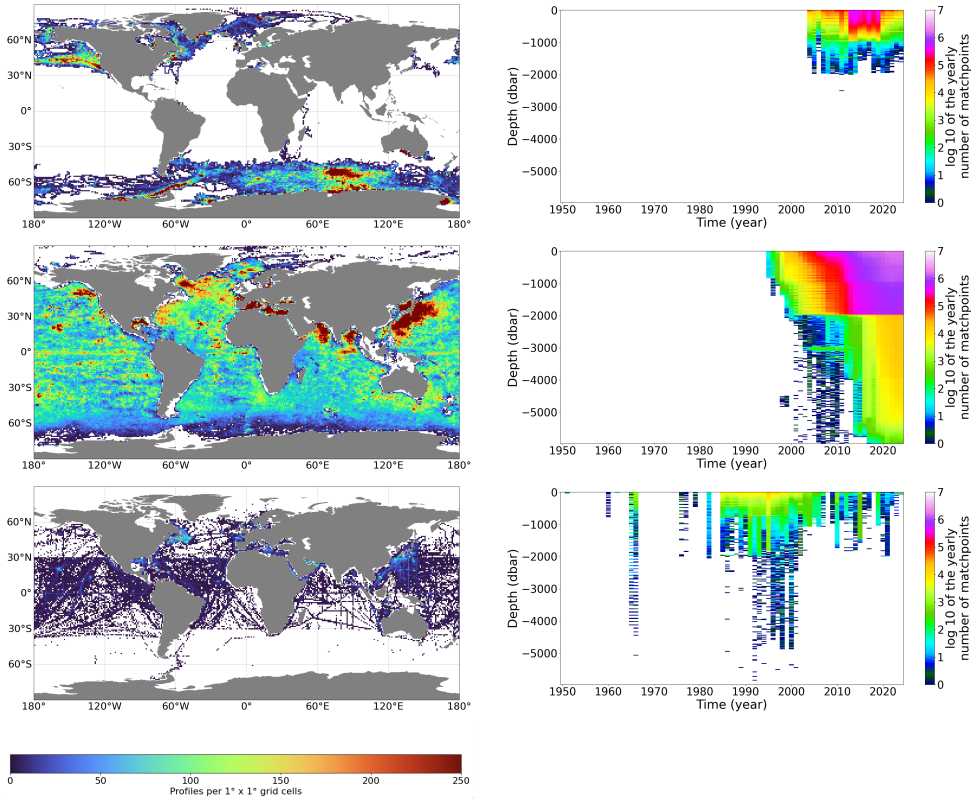


Figure 4. Left: Number of in-situ casts in 1-degree square grid cells from 1950 to 2024. **Right**: Yearly number of measurements in 20-meter vertical depth bins from 1950 to 2024. **Top**: Animal-mounted casts. **Middle**: Autonomous profiler casts. **Bot.**: Unknown type casts.

3 Method

3.1 Data selection and vertical interpolation

Data selection and vertical interpolation are key steps for ensuring the accuracy of the objective analysis. For each month covered by this objective analysis product, the relevant temperature and salinity profiles are extracted from the CORA dataset and assembled into monthly data files. Because the analysis time is centered on the 15th of each month with a 30-day temporal correlation length, successive monthly files necessarily overlap. Only data points with quality-control flags of *good* or *probably good* (QC = 1 or 2) are retained.

To filter the observations, temperature and salinity profiles are compared to the climatological field described in Section 3.2. Equations 1 and 2, for temperature and salinity respectively, are designed to detect data points that deviate from the climatology, with relaxed constraints in regions of high vertical variability. Data points that do not meet these conditions are flagged as bad before the vertical interpolation step. T_{clim} and S_{clim} are the first-guess fields described in Section 3.2, and T_{STD} and S_{STD} the gridded temperature and salinity standard deviation fields of the ISAS17 climatology (Kolodziejczyk et al., 2019). . In this

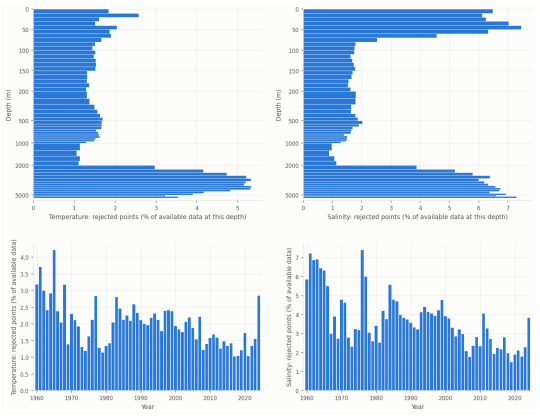


Figure 5. Percentage of good and probably good (QC 1–2) CORA measurements rejected by Eq. 1 (temperature, left) and Eq. 2 (salinity, right), as a function of depth (top) and year (bottom), 1960–2024.

version of CORA OA, we have set $\alpha = 6$ and $\beta = 2$ m, consistently with the parameterization of Kolodziejczyk et al. (2019). Fig. 5 shows that this method flags 1.63% of the good and probably good temperature measurements and 2.58% of the good and probably good salinity measurements. The higher prevalence of flags below 2000 m depth, for both temperature and salinity, is probably a consequence of the lower reliability of the climatologies and of the very low temperature and salinity standard deviations at greater depths. The higher prevalence of flagged salinity measurements in the upper 70 m reflects the difficulty of the WOA23 climatologies in accurately representing coastal ocean variability. In the upper 70 m, 95% of the rejected salinity measurements (97% of those saltier and 91% of those fresher than the climatology) are located within 200 km of the coast, a band that covers only 13% of the ocean surface.

$$|T - T_{clim}| < \alpha T_{STD} + \beta |\frac{dT_{clim}}{dz}| \tag{1}$$

$$|S - S_{clim}| < \alpha S_{STD} + \beta |\frac{dS_{clim}}{dz}| \tag{2}$$

Finally, the observed profiles must be interpolated onto the 186 vertical levels of the objective analysis. The scheme is a standard linear interpolation using only data points flagged as good or probably good (i.e., parameter and pressure/depth quality control flags lower than 3). To account for the reduced accuracy of interpolated values, the measurement error is increased when the observations bracketing a level are far apart compared with the grid spacing (Gaillard et al., 2016; Kolodziejczyk et al., 2019). For each interpolated value, we compute the ratio

$$r = \frac{\Delta z_{obs}}{\Delta z_{grid}}, \tag{3}$$

where Δz_{obs} is the distance between the two observations bracketing the level and Δz_{grid} the local grid spacing. The measurement error standard deviation $\sigma_{M,i}$ is unchanged for $r \leq 2$, and multiplied by 4, 9 and 16 for $2 < r \leq 4$, $4 < r \leq 8$ and

$8 < r \leq 16$, respectively, i.e. its variance $\sigma^2_{M,i}$ in R_{ii} (Eq. 7) is multiplied by 16, 81 and 256. Values with $r > 16$ are discarded.

The objective analysis (OA) then further filters the validated data to remove observations that deviate from the reference field. The method developed by Bretherton et al. (1976) requires prior knowledge of the statistical characteristics of the interpolated field. In the case of CORA OA dataset, this filtering step is designed to remain consistent with mesoscale variability, imposed by the covariance parameterization of the objective analysis (Sect. 3.3), particularly in the deep ocean. Observations that differ from estimated thresholds from the reference are filtered out to avoid propagating small-scale dynamics into the sub-mesoscale analysis.

3.2 Climatology

In the objective analysis framework presented by Bretherton et al. (1976) and further developed into the In Situ Analysis System (ISAS) tool by Gaillard et al. (2016), the analysis is performed on temperature and salinity anomalies relative to reference fields. The choice of these reference fields is therefore crucial for minimizing the objective analysis error. Moreover, during the 1960–2005 period, in-situ profiles did not cover most of the global ocean. Consequently, the analysis converges toward a solution close to the measurements in regions with good observational coverage, but tends toward the climatology in poorly sampled areas. Climatologies covering decadal periods have been used as first guesses in previous versions of the objective analysis (Szekely, 2024a) despite the fact that this approach introduces discontinuities between the end of one climatology and the beginning of the next one. This was particularly evident in the integrated metrics such as global ocean heat content that were biased by the first-guess climatology and failed to represent the detectable effects of long-term warming.

To ensure a smooth temporal evolution of water-mass properties, the first guess of the present version evolves in time. It is derived from the seven WOA23 decadal climatologies covering 1955-1964, 1965-1974, 1975-1984, 1985-1994, 1995-2004, 2005-2014 and 2015-2022 (Reagan et al., 2024). Since these climatologies are monthly, the field of month m of a decadal climatology is the mean of that month over the years of the period. It is therefore assumed to be representative of the central year of the period, i.e. midway between month m of years 1969 and 1970 for the 1965–1974 climatology, and midway between month m of years 2018 and 2019 for the 8-year 2015–2022 climatology. For a month m of year a, the first guess is the linear interpolation between the fields of month m of the two surrounding climatologies k and $k+1$:

$$x_{ref}(a,m) = (1-w)\,C_k(m) + w\,C_{k+1}(m), \qquad w = \frac{a-a_k}{a_{k+1}-a_k}, \tag{4}$$

where $C_k(m)$ is the field of month m of climatology k and a_k its central year (1959.5, 1969.5, …, 2009.5, and 2018.5 for 2015-2022). For example, the January 1973 first guess is obtained with $w = 0.35$ between the January fields of the 1965-1974 and 1975-1984 climatologies. After mid-2018, the first guess is kept equal to the 2015-2022 climatology. Below 1500 m, where WOA23 provides no monthly fields, the seasonal fields are used in Eq. (4) instead of the monthly ones, the field of the season containing month m being used for $C_k(m)$. The anomalies mapped by the objective analysis (Eq. 5) are computed relative to this first guess.

3.3 Objective analysis

3.3.1 Method

Following Gaillard et al. (2016), the analysed field x_a is obtained by adding to the first guess x_{ref} (Eq. 4) a linear combination of the innovations, i.e. the differences between the observations and the first guess at the observation locations:

$$x_a = x_{ref} + K\left(y - Hx_{ref}\right), \tag{5}$$

where y is the vector of observations and H the operator that interpolates the gridded field onto the observation locations. The gain matrix K is

$$K = C_{ao}\left(C_{oo} + R\right)^{-1}, \tag{6}$$

where C_{ao} is the covariance matrix between the grid points and the observation locations, and C_{oo} the covariance matrix between observation locations. R is the observation error covariance matrix, assumed diagonal. Its diagonal elements

$$R_{ii} = \sigma^2_{UR,i} + \sigma^2_{M,i} \tag{7}$$

are the sum of the variance $\sigma^2_{UR,i}$ of the scales not resolved by the analysis (representativeness error) and of the measurement error variance $\sigma^2_{M,i}$ of observation i, possibly increased by the vertical interpolation (Sect. 3.1). C_{ao} and C_{oo} are computed from the covariance function

$$C(dx, dy, dt) = \sum_{j=1}^{2} \sigma^2_{L,j} \exp\left(-\frac{dx^2}{2L^2_{x,j}} - \frac{dy^2}{2L^2_{y,j}} - \frac{dt^2}{2L^2_{t,j}}\right), \tag{8}$$

where dx, dy and dt are the zonal, meridional and temporal distances, $L_{x,j}$, $L_{y,j}$ and $L_{t,j}$ the corresponding correlation scales, and $\sigma^2_{L,j}$ the variance of each component. The spatial scales of the first component ($L_{x,1}$, $L_{y,1}$) are set to 300 km; those of the second component are proportional to the Rossby radius of the first baroclinic mode. Both temporal scales $L_{t,1}$ and $L_{t,2}$ are set to 30 days. These parameters follow Gaillard et al. (2016).

3.3.2 Data distribution and statistics

Fig.6 (Top) shows the amount of data available in each file and at each vertical level. The step-like patterns in data density observed above 1000 m and 2000 m depth before 1990 reflect the nature of data distribution during that period. Most deep profiles available at that time were bottle casts, characterized by very low vertical resolution (see Fig.2, Top Right). The vertical interpolation algorithm described in Section 3.1 tends to eliminate interpolated values that are too far from the original observation points. This pattern tends to disappear as bottle casts were complemented by other observation types after 1990. The vertical interpolation criterion described in Eq. 3 is therefore a likely contributor to this artefact, and will be revised in future versions of the dataset in order to reduce this problem. After the 2000s, data density is dominated by Argo profiles, with

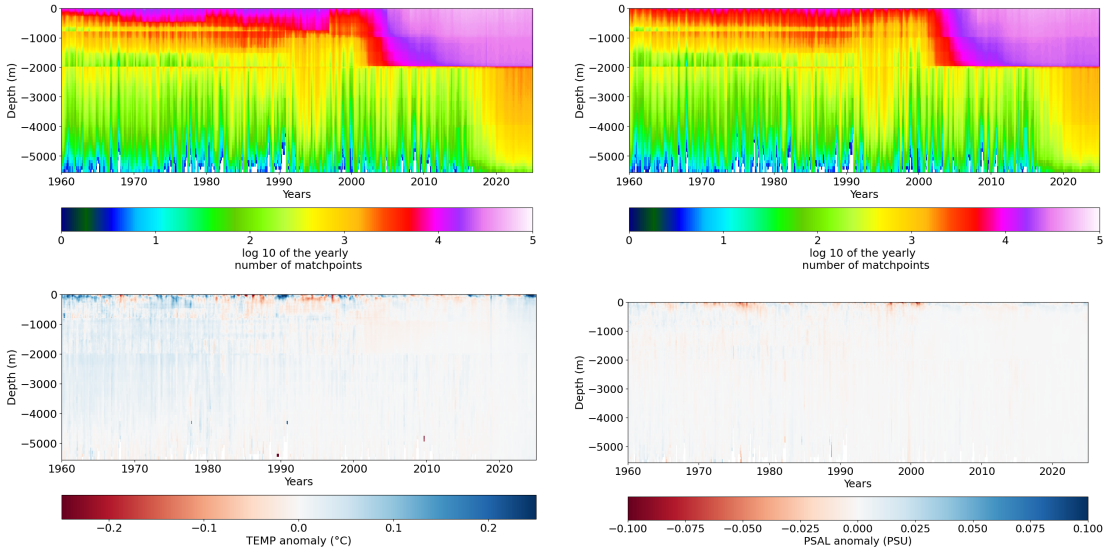


Figure 6. Top: $\log_{10}$ of the number of data points per month and per vertical level in the objective analysis files. Bottom: Monthly median difference between the observations, interpolated onto the analysis levels, and the first guess (innovation). Left: Temperature; Right: Salinity.

a sharp decrease near 2000 m depth corresponding to the maximum profiling depth of most early Argo floats. This limitation was reduced after 2016 with the wider deployment of Deep Argo floats.

Fig. 6 (bottom) shows the monthly median of the innovation $d = y - Hx_{ref}$ (Eq. 5), i.e. the difference between the observations, after vertical interpolation onto the analysis grid, and the first guess (Sect. 3.2) at the same locations. Above 1000m depth, the median anomaly reaches amplitudes over 0.1 °C, decreasing over time, with alternating patches of positive and negative values. This behavior is expected, as the linear interpolation of climatologies cannot capture the interannual variability of ocean temperature. Below 1000m depth, the median anomaly is predominantly negative, with a decreasing amplitude over time. Table 2 shows that the mean temperature anomaly decreases from 0.006 °C in the 0–500m depth layer to 0.004°C in the 2001–5500m layer. Occasional larger anomalies at depth are associated with months where very few profiles are available, and are therefore statistically insignificant. The median salinity anomaly (see table 3) is higher above 500m depth, with significant temporal variations. As expected, the noise decreases over time below 1000m depth.

	5^{th} percentile	Mean	95^{th} percentile
0-500 m depth	-0.08	0.006	0.1
501-1000 m depth	-0.02	0.003	0.04
1001-2000 m depth	-0.009	0.004	0.03
2001-5500 m depth	-0.004	0.004	0.02

Table 2. Mean, 5th and 95th percentiles of the difference between the temperature observations and the first guess, by depth layer. Unit: °C

	5^{th} percentile	Mean	95^{th} percentile
0-500 m depth	-0.03	0.002	0.01
501-1000 m depth	-0.004	0.0001	0.004
1001-2000 m depth	-0.003	-0.0002	0.002
2001-5500 m depth	-0.001	-6×10^{-6}	0.002

Table 3. Mean, 5th and 95th percentiles of the difference between the salinity observations and the first guess, by depth layer. Unit : PSU

3.4 Comparison datasets

Three in-situ 3D gridded products and two surface gridded products are used to evaluate the objective analysis results. Hereafter, IAPv4 will refer to the IAPv4 ocean temperature and salinity dataset from the Institute of Atmospheric Physics (Cheng et al., 2024a). EN4 will refer to the Met Office Hadley EN4 ocean temperature and salinity objective analysis dataset (Good et al., 2013; Killick, 2021). ISAS 20 will refer to the ISAS 20 Argo objective analysis (Kolodziejczyk et al., 2023), which is an analysis performed at the Laboratoire d'Océanographie Physique et Spatiale (LOPS, UMR 6523) using the same tool as the CORA products, but with Argo floats only. ERSST will refer to the extended reconstructed sea surface temperature dataset (version 6) by NOAA (Huang et al., 2025). SSS L4 will refer to the satellite-based SSS product (Sammartino et al., 2022). This product was preferred over other SSS products since its combined in-situ/satellite and SST/SSS approach allows it to extend its time coverage back to 1993, in contrast to products based solely on satellite-measured SSS (e.g., from L-band radiometry missions such as SMOS, Aquarius, or SMAP), which only cover the 2010-2025 period.

4 Results

4.1 SST trend

The upper layer of the CORA OA mean temperature anomaly time series is compared with three international reference 3D datasets (IAPv4, EN4, and ISAS 20) and one SST dataset (ERSST) (Figure 7). All SST averages are computed between 60 °S and 60 °N, which excludes the regions covered by sea ice. All time series in Figure 7 are expressed as anomalies relative to their mean over the period common to all products (2002-2020), so that differences in absolute level and in temporal coverage do not affect the comparison. Trends are computed over the available period of each product, and are therefore directly comparable only between products of identical coverage. The sea surface warming trend value and the associated 90% confidence interval shown by all products are calculated using a LOWESS method (Cheng et al., 2022a). In all basins, the CORA mean SST warming rate falls within the range of the warming rates of the other products. The agreement between products is very good in the global ocean and in the Atlantic basin. However, there are discrepancies: EN4 shows a lower temperature anomaly in the Pacific, Indian, and Southern Oceans during 2005–2022, and ERSST shows lower anomalies during 1960–1970 in the same basins. In addition, CORA appears to exhibit lower interannual variability, particularly in the Southern Ocean and Indian

Ocean, despite the good overall agreement in the tendency. These regions also show limited data availability across all data types compared with the Atlantic Ocean and the North Pacific (see Figures 2 and 4). We can therefore assume that the reduced interannual variability is partly a consequence of the scarcity of available profiles. However, the CORA OA product also exhibits low interannual variability after 2005, when the Argo program reached near-global coverage. It is then possible that this smoothed interannual variability results from the specific parameterization of the correlation function used in the objective analysis (see Equation 8).

In all basins, the IAPv4 warming trend lies at the lower end of the range spanned by the products, while the CORA trend tends to lie at the upper end. This is likely due to EN4, CORA, and ERSST that include the years 2023 and 2024, which exhibit record-high global sea surface temperature anomalies (Huang et al., 2024; Terhaar et al., 2025). When restricting the calculation of warming trends to years prior to 2023, the spread among products is reduced: CORA: 0.93 $\pm$ 0.06°C/century, ERSST: 0.93 $\pm$ 0.23°C/century, EN4: 0.87 $\pm$ 0.23°C/century, IAPv4: 0.79 $\pm$ 0.27°C/century, ISAS20: 1.0 $\pm$ 0.7°C/century. In this case, only ISAS20 departs from the other analyses, but it covers only 2002–2020, a period during which the ocean warming rate is higher than before the 2000s (Cheng et al., 2022b). In nearly all comparisons, the ERSST warming rate diverges from other products, since ERSST mean temperatures are systematically lower than any other datasets in all basins during the 1960s. Conversely, the CORA warming rate shows smaller 90% confidence interval than other products, likely due to the lower interannual variability of the CORA OA time series, particularly before the Argo era. The ocean basin with the largest spread in mean SST time series is the Southern Ocean (35–60 °S). In this basin, all products except ERSST show overall good agreement until 2000. After that, the spread increases: EN4 and ISAS20 provide the lowest estimates, IAPv4 and ERSST the highest, while CORA remains close to the median. In this basin, the lack of data prior to the 2000s is striking (see Fig. 2). This situation improved in the 2000s with the development of Argo floats and the use of animal-mounted CTDs (see Fig. 4). Although animal-mounted CTDs provide valuable profiles, they are prone to data drift and sensor malfunctions due to challenging deployment conditions. The CORA validation process efficiently detects and flags failed instruments, thereby reducing the influence of sensor drift (Szekely et al., 2019; Szekely, 2024b), however, we cannot compare our profile selection with that used by other products. Consequently, it is difficult to determine whether the spread among products is driven by differences in data availability, data validation, or first guesses.

4.2 SSS trend

The upper layer of the CORA OA salinity analysis is compared to the EN4, ISAS 20, and IAPv4 upper layers, as well as to the SSS L4 product (Figure 8). This comparison is limited to regions where the bathymetry exceeds 1500 m, in order to reduce the influence of low-salinity coastal areas, which are more pronounced in the higher-resolution products (SSS L4 and IAPv4) than in the others. At the global scale and across all ocean basins, the CORA product generally aligns more closely with EN4 than with IAPv4 during the pre-Argo era. An exception occurs in the late 1990s, when the EN4 signal rises to the level of the IAPv4 product for the Global Ocean (0.02 PSU difference), Atlantic Ocean (0.05 PSU), and Pacific Ocean (0.03 PSU). During this period, the CORA signal is closer to the SSS L4, with no sign of SSS sharp variation. The spread among products decreases during the Argo era (2005–present), with all datasets showing good agreement, especially after 2010, thanks to greater data

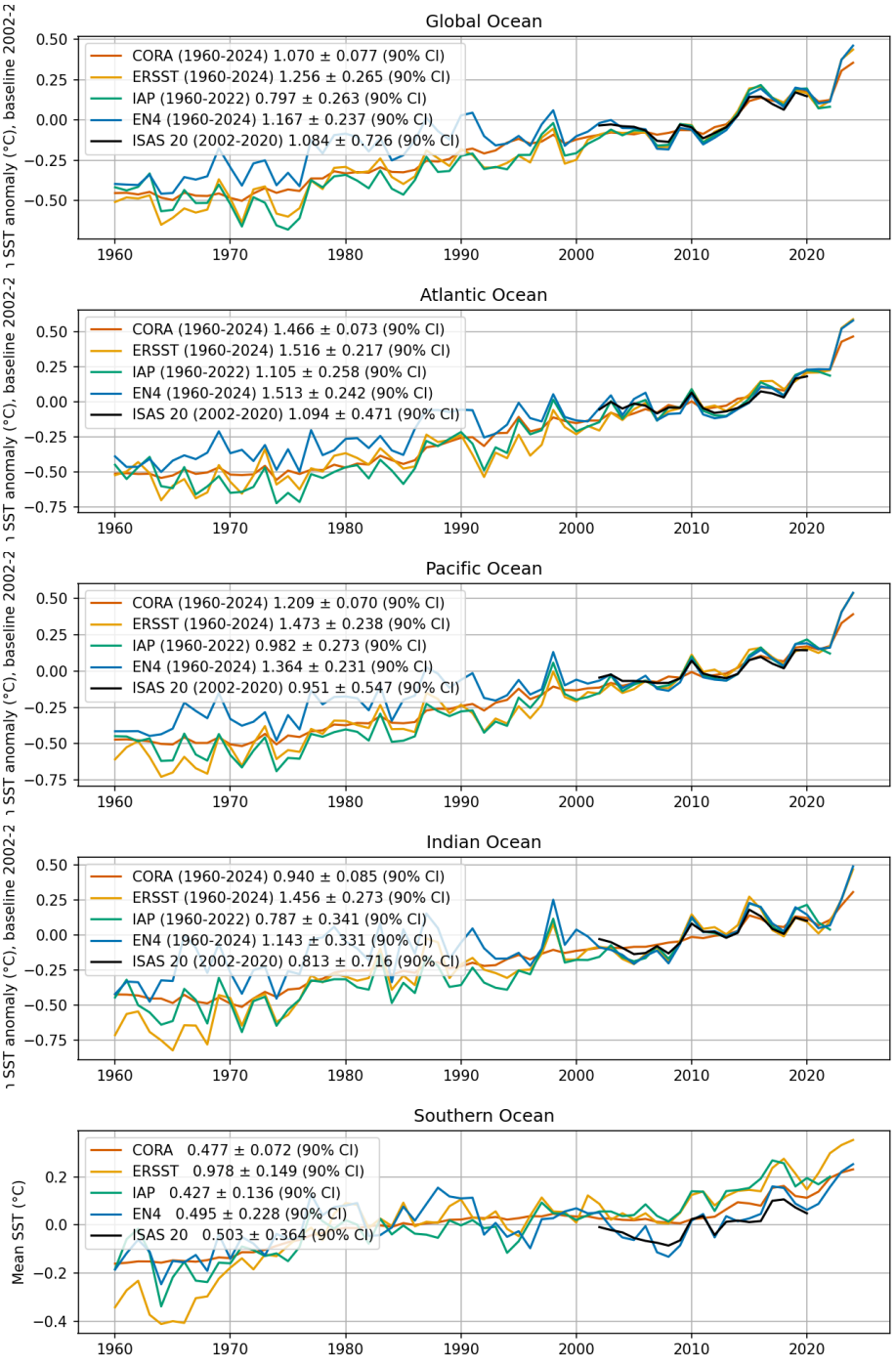


Figure 7. Mean SST and trends for CORA, EN4, IAPv4, ERSST, and ISAS 20 for the global ocean, Atlantic Ocean, Pacific Ocean, Indian Ocean, and Southern Ocean (35–60 °S). All averages are computed between 60 °S and 60 °N.

		1960–1984	1985–2005	2006–2020
CORA	Global	0.018	0.018	0.026
	Pacific	0.020	0.024	0.023
	Atlantic	0.022	0.033	0.025
	Indian	0.022	0.018	0.031
	South	0.005	0.004	0.020
EN4	Global	0.067	0.065	0.058
	Pacific	0.076	0.073	0.060
	Atlantic	0.065	0.077	0.060
	Indian	0.110	0.100	0.077
	South	0.050	0.039	0.051
ERSST	Global	0.069	0.061	0.057
	Pacific	0.076	0.077	0.057
	Atlantic	0.077	0.081	0.051
	Indian	0.095	0.095	0.084
	South	0.041	0.041	0.039
IAP v4	Global	0.072	0.059	0.059
	Pacific	0.072	0.079	0.063
	Atlantic	0.069	0.084	0.061
	Indian	0.100	0.095	0.078
	South	0.062	0.038	0.040
ISAS 20	Global	–	–	0.045
	Pacific	–	–	0.044
	Atlantic	–	–	0.042
	Indian	–	–	0.057
	South	–	–	0.032

Table 4. Detrended standard deviation of the SST by ocean basin and by sub-period (unit: °C)

	1960–1984	1985–2005	2006–2020
ERSST	0.069	0.060	0.046
IAP	0.081	0.060	0.045
EN4	0.074	0.082	0.046
ISAS 20	–	–	0.026
SSS L4	–	–	–

Table 5. SST RMS differences (unit: °C)

availability. An exception is the consistently higher salinity values in the EN4 product in the Southern Ocean. In this basin, CORA converges toward IAPv4 after 1985 and shows very good agreement with all products except EN4 in the 2000s which exhibits higher mean salinity with the discrepancy widening after 2015. A closer inspection of the monthly surface salinity fields reveals that the large negative anomaly in 2001 in the IAPv4 product originates from a well-defined, large-scale feature located in the eastern Indian Ocean and the western Pacific Ocean, with amplitudes exceeding -1 PSU relative to the 2004-2010 level. This anomaly pattern and amplitude are unique to the IAPv4 product during this specific period and are not found in the other SSS products used in this study, suggesting that it reflects a product-specific artifact in IAPv4 rather than a genuine

oceanographic signal. For SSS, as for SST, CORA displays lower interannual variability than the other reference products, although the long-term variability remains very similar. This finding is consistent with what was reported for SST in Section 4.1. In the case of SSS, the reduced interannual variability of CORA is likely influenced by the 30-day time scale used in the correlation function (see equation8). This time scale is longer than the characteristic variability of large river plume systems, even in open-ocean regions (Fournier et al., 2017; Varona et al., 2019; Boutin et al., 2021; Shi and Wang, 2024).

		1960–1984	1985–2005	2006–2020
CORA	Global	0.0017	0.0029	0.0035
	Pacific	0.0029	0.0018	0.0065
	Atlantic	0.0038	0.0035	0.0074
	Indian	0.0031	0.0010	0.0089
	South	0.0007	0.0009	0.0017
EN4	Global	0.0060	0.0086	0.0073
	Pacific	0.010	0.013	0.012
	Atlantic	0.015	0.016	0.011
	Indian	0.0154	0.016	0.017
	South	0.0048	0.0062	0.0061
IAP v4	Global	0.0075	0.010	0.0053
	Pacific	0.016	0.013	0.010
	Atlantic	0.019	0.015	0.0094
	Indian	0.017	0.027	0.016
	South	0.013	0.0048	0.0051
ISAS 20	Global	–	–	0.0062
	Pacific	–	–	0.0095
	Atlantic	–	–	0.0086
	Indian	–	–	0.015
	South	–	–	0.0030
SSS L4	Global	–	–	0.0067
	Pacific	–	–	0.013
	Atlantic	–	–	0.011
	Indian	–	–	0.017
	South	–	–	0.0043

Table 6. Detrended standard deviation of the SSS by ocean basin and by sub-period (unit: PSU)

Table 4 and 6 give the detrended standard deviation of the SST and SSS time series for all tested products and for three periods. It shows that CORA almost always gives a lower estimate of the detrended SSS or SST variability, by a factor of 2 to 10. The most severe underestimation occurs before the Argo era in the Southern Ocean, and the gap narrows markedly during the Argo era. It is consistent with a damping of the objective-analysis signal in regions and periods where data coverage is sparse. The comparison also shows that ISAS20 underestimates the detrended standard deviation relative to the other products, though to a lesser extent than CORA. This is likely related to the linear vertical interpolation scheme shared by CORA and ISAS20 (see Section 3.1), which does not extrapolate to the surface for profiles whose shallowest observation lies below 1 m depth, reducing the number of valid surface data points relative to the other products. The residual gap between CORA and ISAS20 likely reflects a difference in data sources: ISAS20 uses the full Argo profiles from the Global Data Assembly Center,

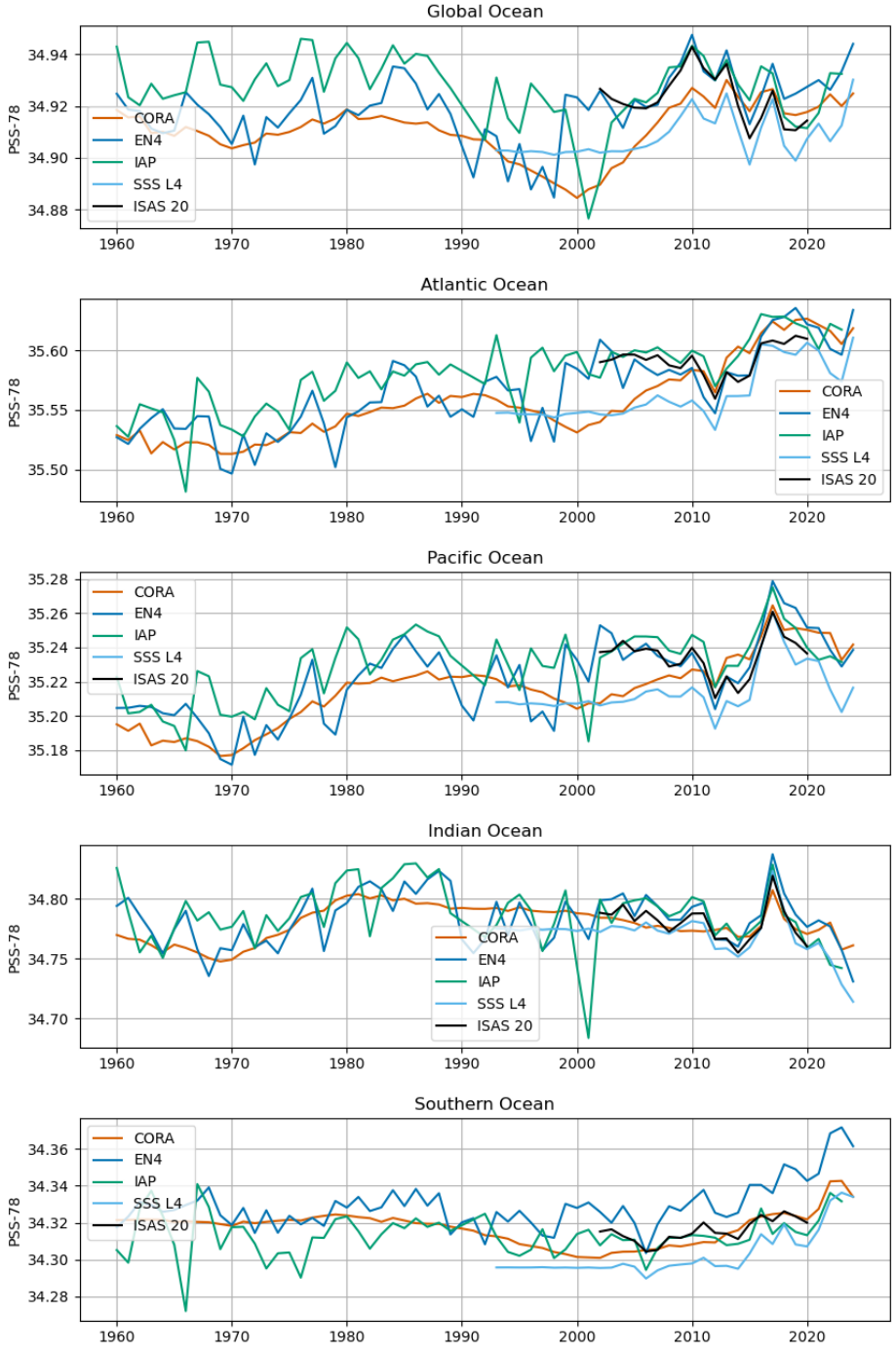


Figure 8. Mean SSS in deep ocean zones (bottom depth $>$ 1500 m) for CORA, EN4, IAPv4, SSS L4, and ISAS 20 for the global ocean, Atlantic Ocean, Pacific Ocean, Indian Ocean, and Southern Ocean (south of 35 °S).

whereas CORA discards Argo sub-surface measurements taken while the CTD pump was not activated, further reducing the number of valid near-surface observations available to CORA relative to ISAS20.

	1960–1984	1985–2005	2006–2020
ERSST	–	–	–
IAPv4	0.0081	0.011	0.0071
EN4	0.0063	0.015	0.0061
ISAS 20	–	–	0.0086
SSS L4	–	–	0.0050

Table 7. SSS RMS differences (unit: PSU)

Tables 5 and 7 give the RMS differences between CORA and the reference products. The SST RMS difference decreases with time for ERSST and IAPv4, and slightly increases then decreases for EN4. ERSST, IAPv4 and EN4 SST RMS differences are almost identical during the Argo era, While that of ISAS20 is smaller by a factor of $\sim$1.8. This suggests that the objective-analysis method shared by ISAS20 and CORA tends to produce more consistent interannual variability between the two than either does with the other products. The SSS RMS difference (for IAPv4 and EN4, the only products with data across all three periods) is low during both the early period and the Argo era, and peaks during 1985-2005, consistent with the late-1990s and 2001 discrepancies described above.

4.3 OHC estimation

In addition to being a key indicator for understanding the evolution of the Earth's climate (Meyssignac et al., 2019; Pan et al., 2025), the intercomparison of OA products also provides a means to assess the robustness of individual products and the consistency of their temperature fields (e.g. Liang et al., 2021). The CORA OA global ocean heat content (GOHC) is compared with the estimate of the US National Centers for Environmental Information (NCEI) (Levitus et al., 2012), an estimate based on IAPv4 (Cheng et al., 2024b), and the estimate of the Global Climate Observing System (GCOS) initiative (von Schuckmann et al., 2023). GOHC is integrated over the 0-2000 m layer and between 60 °S and 60 °N, which excludes most sea-ice-covered regions. NCEI and IAPv4 GOHC were recomputed over this domain from their gridded fields. The GCOS estimate is only available as a global integral. The NCEI 0-2000 m estimate is only available as pentadal (5-year) means before 2005 (Levitus et al., 2012). The products are originally provided relative to different reference periods (2005-2020 for CORA OA and IAPv4, 1955-2006 for NCEI, and 1960 for GCOS). All series are therefore re-referenced to the common 2005-2020 baseline by removing, from each annual series, its own 2005-2020 mean. Statistics are computed from annual means over three sub-periods common to all products (1960-1984, 1985-2005 and 2006-2020), the recent period being limited to 2020 by the GCOS record. Trends are estimated by linear least-squares regression, the quoted uncertainty being the standard error of the slope, and standard deviations are computed on linearly detrended series within each sub-period.

All GOHC time series (Fig. 9) agree within their uncertainties after 1995. During the Argo era, CORA OA is slightly lower than the other products (by 5-10 ZJ over 2008-2016) and displays larger interannual fluctuations. During 1975-1995 the four estimates are within 20 ZJ of each other, except for a 20-30 ZJ positive departure of NCEI around 1990–1994. The largest discrepancies occur during 1960-1975. Relative to the common baseline, NCEI, GCOS and IAPv4 decrease from about -240 ZJ in 1960 to a minimum of -255 to -265 ZJ around 1968-1970, whereas CORA OA remains nearly flat between -200 and -220 ZJ, that is, 30-50 ZJ above the other products, although within its uncertainty range. This offset is the counterpart of the lower CORA OA trend over 1960-1984 (1.8 ± 2.7 ZJ yr^{-1}, compared with 2.3-3.3 ZJ yr^{-1} for the other products; Table 8). These results are consistent with Lyman and Johnson (2008) and Cheng and Zhu (2014a), who showed that OHC time series and their uncertainties are sensitive to the OA first guess and to the data distribution. The GOHC of the CORA OA first guess alone (Fig. 9, dashed line) shows that the CORA product closely follows the first guess estimation during the 1960-1985 and the 2005-2018 period and shows an order -10 to -30 ZJ anomaly during the 1985-2005 period. It completely differs from the first guess after 2018 since the first guess field is maintained constant after 2018.

When compared with basin-scale estimates from NCEI (not shown), the 1960-1984 positive offset of CORA OA is clear in the Atlantic Ocean but almost undetectable in the Pacific and Indian Oceans. Data coverage during this period was much higher in the Atlantic than in the Indian and Pacific Oceans, which suggests that this feature may reflect a bias in the data. As most of the profiles from this period are bottle casts, the potential impact of the linear vertical interpolation scheme cannot be neglected: Li et al. (2022) showed that linear interpolation of profiles tends to overestimate GOHC by about 40 ZJ before 1990.

	1960-1984	1985-2005	2006-2020
CORA OA	1.8 ± 2.7	6.4 ± 1.6	10.1 ± 1.5
NCEI	3.3 ± 4.5	5.1 ± 1.2	10.8 ± 1.4
GCOS	2.3 ± 2.1	6.2 ± 1.4	9.8 ± 0.9
IAPv4	2.6 ± 1.3	6.2 ± 4.6	8.9 ± 0.6
First guess	2.1 ± 2.1	5.7 ± 1.3	9.0 ± 2.2

Table 8. Linear trend (ZJ yr^{-1}) of the 0-2000 m global ocean heat content, integrated between 60 °S and 60 °N (GCOS: global integral). NCEI trends before 2005 are computed from pentadal means. Uncertainties are the standard error of the slope.

Table 9 shows that the detrended interannual variability of GCOS and IAPv4 decreases from about 14-16 ZJ in 1960-1984 to 5.8-7.2 ZJ in 2006-2020. CORA OA, by contrast, has a lower variability during 1960-1984 (12 ZJ) and a slowly decreasing level afterwards (11.3-8.8 ZJ), comparable to NCEI and above IAPv4 and GCOS in the Argo era. A likely explanation for the low early-period variability of CORA OA is that, where observations are sparse relative to the correlation scales, the analysis increments are small and the analysed fields relax toward the time-evolving first guess, which by construction inhibits interannual variability. The interannual variability of CORA OA before 1985 should therefore be regarded as a lower bound, partly damped toward the WOA23 decadal climatologies. Conversely, the higher early-period variability of the other products may

	1960-1984	1985-2005	2006-2020
CORA OA	12.0	11.3	8.8
NCEI	–	–	8.4
GCOS	16.3	13.0	7.2
IAPv4	14.0	17.5	5.8
First guess	9.5	4.8	7.2

Table 9. Standard deviation (ZJ) of the linearly detrended annual 0–2000 m global ocean heat content anomalies within each sub-period. NCEI values are not given before 2005, since only pentadal means are available.

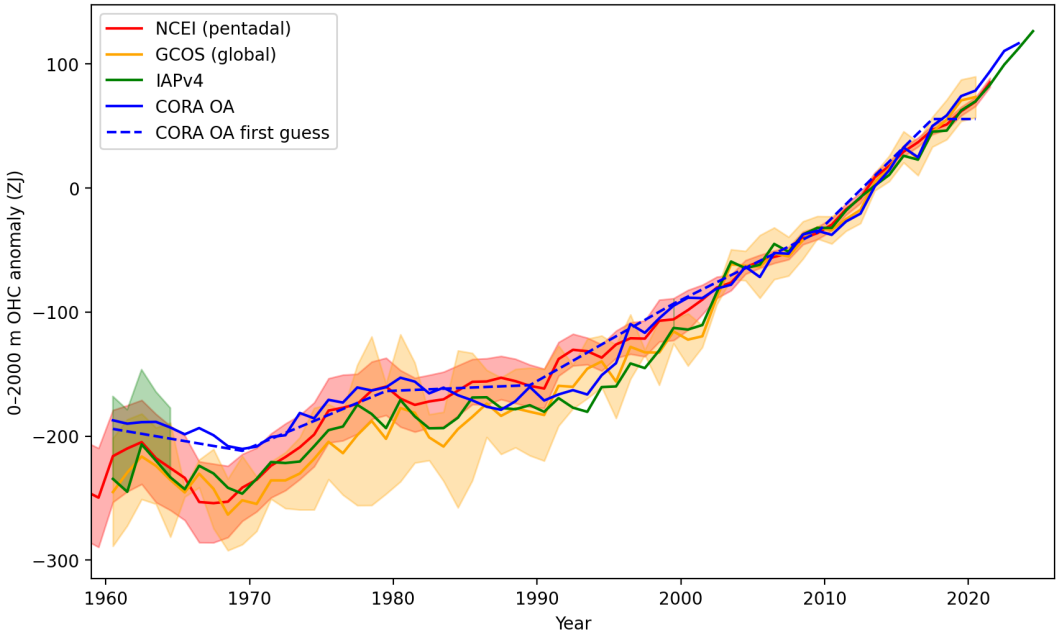


Figure 9. Annual 0-2000 m global ocean heat content anomaly (ZJ) for CORA OA, IAPv4 and NCEI (pentadal means before 2005) and CORA OA first guess, integrated between 60 °S and 60 °N, and for GCOS (global integral). All series are referenced to their 2005-2020 mean. Shading: 95 % uncertainty range : ±1.96 standard error.

partly reflect sampling noise, but this cannot be established from the present comparison alone. In the Argo era, the differences in variability levels between products are consistent with differences in the effective smoothing of their mapping methods.

4.4 Steric sea level

The analysis of the mean steric sea level anomaly is key indicator for monitoring the "salty drift" of Argo floats (Liu et al., 2024), first identified by Wong et al. (2020). This drift affects a large fraction of Argo floats, introducing a small positive salinity

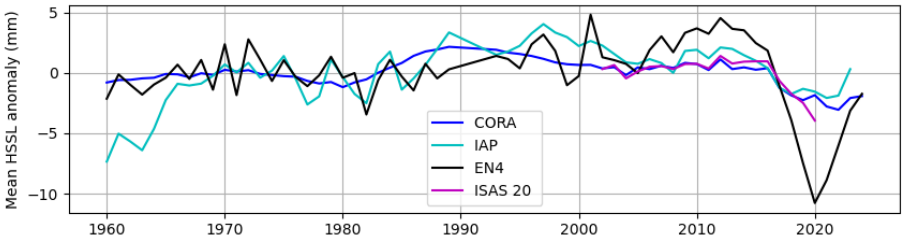


Figure 10. Mean halosteric height anomaly (60 °S-60 °N, 0-2000 m) for CORA, ISAS 20, IAPv4 and EN4.

bias. Although this bias is difficult to detect and correct, its impact becomes apparent in halosteric anomaly calculations, which integrate even small errors from deep layers to the surface. Later, the Argo community attempted to adjust or flag the spurious profiles (Wong et al., 2023), but some effect of the salty drift remains in the 2D gridded fields (Tang et al., 2024; Liu et al., 2024).

Figure 10 shows the time series of the yearly mean halosteric height anomaly (HSSLA) calculated following equation 9, with β_S the saline contraction coefficient and h the maximum depth of the integration, set to 2000 m depth. Anomalies are computed relative to the 2005-2020 mean of each product. The CORA product exhibits long-term variability similar to EN4 and IAPv4, although with lower interannual variability. The Argo salty drift contributes to a spread among the products, as noted by Liu et al. (2024). Following the assumptions of Wong et al. (2020), this spread might decrease after 2022, as the number of Argo profilers with delayed-time mode adjustments increase and the manufacturing issue responsible for the salty drift has been partly resolved. The ISAS 20 products exhibit variability very similar to CORA, although with a sharp decrease in HSSLA in 2018–2020. This is likely because the ISAS 20 product, produced in 2021, included fewer Argo floats with delayed-time mode adjustments for those 3 years.

$$\mathrm{HSSL} = -\int_{-h}^{0} \beta_S \left(S - \bar{S}\right) dz \tag{9}$$

5 Conclusions

The updated version of the CORA OA product (INSITU_GLO_PHY_TS_OA_MY_013_052 in the Copernicus Marine Service catalogue) now spans the period 1960–2024 and the depth range 0–5500 m. It is based on all available in-situ profiles distributed through the INSITU_GLO_PHY_TS_DISCRETE_MY_013_001 product (CMEMS, 2025). The objective analysis method relies on the ISAS-V6 algorithm (Gaillard et al., 2016). This work details the objective mapping approach and associated parameters, with a particular focus on defining an appropriate first-guess field to ensure accurate estimates of global ocean heat content.

The product is validated by comparing it with a selection of international reference fields. Parameters such as SST and SSS are evaluated against both in-situ–based gridded products and satellite-derived products. Integrated quantities, including halosteric sea-level anomaly and global ocean heat content, are also assessed to ensure that, once vertically interpolated, the gridded product remains accurate.

The SST validation shows that the objective analysis is in very good overall agreement with the reference products. Global trends are consistent with these references, both at the global scale and at individual basin scales. However, the objective-analysis parameters tend to smooth interannual variability, meaning that this time scale is not well represented in the product—particularly before the Argo era and in sparsely sampled regions. The definition of the correlation function necessarily involves a compromise among large-scale, mesoscale, and unresolved processes. As a result, the effective correlation scale depends on the local and temporal density of ocean observations and should therefore vary substantially in space and time.

The SSS comparison also shows good agreement between CORA OA and the reference products at both global and basin scales, although differences in grid resolution and in the representation of river plumes lead to a large spread among products. This spread decreases markedly with the development of the Argo program and the sharp increase in data availability after 2005.

The analysis of the steric sea-level time series also shows good overall agreement with the reference products. The impact of the Argo fast-salinity drift after 2016 appears to be more limited in this product than in the others and comparable to IAPv4. This is likely a consequence of the CORA dataset production process, which places strong emphasis on profile validation and introduces a delay between the actual profile measurement and its inclusion in the CORA objective-analysis framework. The Argo processing system is indeed very effective at detecting, adjusting, and often flagging affected profiles in delayed-time mode (Cabanes et al., 2016), but this procedure can take time. The CORA production strategy, which provides a major update of the whole database each year, ensures that Argo profiles are refreshed on a quarterly basis to remain aligned with the most recent Argo data modes. In contrast, the products based on a near real time processing of Argo profiles, such as EN4, often lack the effects of the Argo post processing and exhibit stronger effects of fast salty drift.

Comparisons of global ocean heat content with reference products show good overall agreement after 1975, all estimates lying within 20 ZJ of each other, and within their uncertainties after 1995. The product however appears to overestimate heat content during the 1960s, by 30 to 50 ZJ relative to the other estimates, an offset that vanishes by the mid-1970s. During the Argo era, CORA OA is slightly lower than the other products (by 5–10 ZJ over 2008–2016). The strong correlation between the CORA GOHC anomaly trend and reference products validates the dataset's ability to accurately reflect the impacts of global climate change on marine thermal structures. The effects of the evolution of the Argo data mode on such metric remain unclear, however the pressure correction of Argo floats have shown to have a significant impact on thermosteric level anomaly calculation (Barker et al., 2011), and hence might have an impact of global ocean heat content estimation.

This study demonstrates that although major improvements have been integrated into this new version, further refinements are possible. The most critical priority is the enhancement of the vertical interpolation scheme to reduce the ocean heat content overestimation resulting from the sparse vertical profiles (primarily bottle data) available during this period (Cheng and Zhu, 2014b; Li et al., 2022; Barker and McDougall, 2020). A second key improvement would be the update of the XBT correction

scheme. It must be highlighted, however, that these two points focus on correcting small but systemic bias-inducing errors in large-scale vertically integrated quantities, such as global ocean heat content. At the individual profile scale, these error sources remain low relative to the product's precision; consequently, local temperature and salinity estimations remain accurate in well-sampled regions for these periods.

6 Data availability

This product is based on the November 2025 release of the CORA dataset (CMEMS, 2025)), available at https://doi.org/10.17882/46219#124093. The dataset described in this paper is freely available at https://doi.org/10.48670/mds-00383.

7 Code availability

The Python and Fortran 90 codes used to perform this analysis are openly available under the MIT licence at https://doi.org/10.5281/zenodo.20824880.

Acknowledgements. This study has been conducted using E.U. Copernicus Marine Service. The authors wish to thank the members of the Copernicus Marine Service In Situ Thematic Assembly Centre (In Situ TAC) for their valuable feedback and constructive discussions. The In Situ TAC is coordinated by Ifremer (France) and brings together the expertise of 16 European institutes, including Puertos del Estado, HCMR, IOBAS, IMR, SMHI, BSH, Coriolis, SOCIB, CLS, SYKE, MetOffice, OGS, the University of Bergen, and Azti. Their collective effort in providing consistent, quality-controlled ocean in situ observations greatly supported the present work. The authors would also like to extend their sincere gratitude to Dominique Aubaton for his careful reviews and insightful advice, which greatly contributed to the writing of this manuscript.

The authors declare that AI-assisted tools (Claude, Anthropic and Chat GPT-4, OpenAI) were used during the preparation of this manuscript to improve the grammar, clarity, and accuracy of the text. The scientific content, data analysis, and conclusions remain entirely the responsibility of the authors.

References

Pierre Bahurel, Fabio Adragna, M. J. Bell, Fabrice Jacq, Johnny A. Johannessen, Pierre-Yves Le Traon, Jun She, et al. Ocean monitoring and forecasting core services: The european myocean example. In *Proceedings of OceanObs'09: Sustained Ocean Observations and Information for Society*, volume 2, pages 21–25, Venice, Italy, 2010. ESA Publication WPP-306. URL https://www.researchgate.net/publication/260336424_OceanObs'09_Sustained_Ocean_Observations_and_Information_for_Society. doi available in proceedings.

Paul Barker, Jeff Dunn, Catia Domingues, and Susan Wijffels. Pressure sensor drifts in argo and their impacts. *Journal of Atmospheric and Oceanic Technology - J ATMOS OCEAN TECHNOL*, 28:1036–1049, 08 2011. https://doi.org/10.1175/2011JTECHO831.1.

Paul M. Barker and Trevor J. McDougall. Two interpolation methods using multiply-rotated piecewise cubic hermite interpolating polynomials. *Journal of Atmospheric and Oceanic Technology*, 37(4):605–619, 2020. https://doi.org/10.1175/jtech-d-19-0211.1. URL https://doi.org/10.1175/jtech-d-19-0211.1.

Bernard Bourlès, Rick Lumpkin, Michael J. McPhaden, Fabrice Hernandez, Paulo Nobre, and et al. The pirata program: History, accomplishments, and future directions. *Bulletin of the American Meteorological Society*, 89(8):1111–+, 2008. https://doi.org/10.1175/2008BAMS2462.1.

J. Boutin, N. Reul, J. Koehler, A. Martin, R. Catany, S. Guimbard, et al. Satellite-based sea surface salinity designed for ocean and climate studies. *Journal of Geophysical Research: Oceans*, 126:e2021JC017676, 2021. https://doi.org/10.1029/2021JC017676. URL https://doi.org/10.1029/2021JC017676.

F.P. Bretherton, R.E. Davis, and C.B. Fandry. A technique for objective analysis and design of oceanographic experiments applied to mode-73. *Deep Sea Research and Oceanographic Abstracts*, 23(7):559–582, 1976. https://doi.org/10.1016/0011-7471(76)90001-2.

C. Cabanes, A. Grouazel, K. von Schuckmann, M. Hamon, V. Turpin, C. Coatanoan, F. Paris, S. Guinehut, C. Boone, N. Ferry, C. de Boyer Montégut, T. Carval, G. Reverdin, S. Pouliquen, and P.-Y. Le Traon. The cora dataset: validation and diagnostics of in-situ ocean temperature and salinity measurements. *Ocean Science*, 9:1–18, 2013. https://doi.org/10.5194/os-9-1-2013.

Cécile Cabanes, Virginie Thierry, and Catherine Lagadec. Improvement of bias detection in argo float conductivity sensors and its application in the north atlantic. *Deep Sea Research Part I: Oceanographic Research Papers*, 114:128–136, 2016. ISSN 0967-0637. https://doi.org/https://doi.org/10.1016/j.dsr.2016.05.007. URL https://www.sciencedirect.com/science/article/pii/S0967063715301436.

Piers Chapman. The world ocean circulation experiment (woce). *Marine Technology Society Journal*, 32(3):23, 1998. URL https://www.researchgate.net/profile/Piers-Chapman/publication/256804472_The_World_Ocean_Circulation_Experiment_WOCE/links/587f7ed208ae9275d4ee337d/The-World-Ocean-Circulation-Experiment-WOCE.pdf. Fall 1998; ProQuest.

L. Cheng and J. Zhu. Artifact in variations of ocean heat content induced by the observation system changes. *Geophys. Res. Lett.*, 41: 7276–7283, 2014a. https://doi.org/10.1002/2014GL061881.

L. Cheng, J. Zhu, R. Cowley, T. Boyer, and S. Wijffels. Time, probe type, and temperature variable bias corrections to historical expendable bathythermograph observations. *Journal of Atmospheric and Oceanic Technology*, 31:1793–1825, 2014. https://doi.org/10.1175/JTECH-D-13-00197.1.

L. Cheng, G. Foster, Z. Hausfather, K. E. Trenberth, and J. Abraham. Improved quantification of the rate of ocean warming. *J. Climate*, 35: 4827–4840, 2022a. https://doi.org/10.1175/JCLI-D-21-0895.1.

L. Cheng, K. von Schuckmann, J. P. Abraham, et al. Past and future ocean warming. *Nature Reviews Earth & Environment*, 3:776–794, 2022b. https://doi.org/10.1038/s43017-022-00345-1.

L. Cheng, Y. Pan, Z. Tan, H. Zheng, Y. Zhu, W. Wei, J. Du, H. Yuan, G. Li, H. Ye, V. Gouretski, Y. Li, K. E. Trenberth, J. Abraham, Y. Jin, F. Reseghetti, X. Lin, B. Zhang, G. Chen, M. E. Mann, and J. Zhu. Iapv4 ocean temperature and ocean heat content gridded dataset. *Earth Syst. Sci. Data*, 16:3517–3546, 2024a. https://doi.org/10.5194/essd-16-3517-2024.

L. Cheng, K. von Schuckmann, A. Minière, et al. Ocean heat content in 2023. *Nature Reviews Earth & Environment*, 5:232–234, 2024b. https://doi.org/10.1038/s43017-024-00539-9. URL https://doi.org/10.1038/s43017-024-00539-9.

Lijing Cheng and Jiang Zhu. Uncertainties of the ocean heat content estimation induced by insufficient vertical resolution of historical ocean subsurface observations. *Journal of Atmospheric and Oceanic Technology*, 31(6):1383–1396, 2014b. https://doi.org/10.1175/JTECH-D-13-00220.1. URL https://doi.org/10.1175/JTECH-D-13-00220.1.

CMEMS. Insitu_glo_phy_ts_discrete_my_013_001. https://doi.org/10.17882/46219, 2025. (accessed on 01-12-2025).

Copernicus Marine In Situ TAC partners. Product user manual for in situ products (INSITU_GLO_PHYBGCWAV_DISCRETE_MYNRT_013_030 to INSITU_NWS_PHYBGCWAV_DISCRETE_MYNRT_013_036). Product User Manual CMEMS-INS-PUM-013-030-036, Issue 2.3, Copernicus Marine Service, In Situ Thematic Assembly Centre; Mercator Ocean International, Toulouse, France, November 2025. URL https://documentation.marine.copernicus.eu/PUM/CMEMS-INS-PUM-013-030-036.pdf.

S. Fournier, J. Vialard, M. Lengaigne, T. Lee, M. M. Gierach, and A. V. S. Chaitanya. Modulation of the ganges-brahmaputra river plume by the indian ocean dipole and eddies inferred from satellite observations. *Journal of Geophysical Research: Oceans*, 122(12): 9591–9604, 2017. https://doi.org/https://doi.org/10.1002/2017JC013333. URL https://agupubs.onlinelibrary.wiley.com/doi/abs/10.1002/2017JC013333.

F. Gaillard. Isas-tool version 6: Method and configuration. Technical Report LPO-12-02, Ifremer, 2012. URL https://archimer.ifremer.fr/doc/00115/22582/.

F. Gaillard, E. Autret, V. Thierry, P. Galaup, C. Coatanoan, and T. Loubrieu. Quality control of large argo datasets. *Journal of Atmospheric and Oceanic Technology*, 26:337–351, 2009. https://doi.org/10.1175/2008JTECHO552.1.

F. Gaillard, T. Reynaud, V. Thierry, N. Kolodziejczyk, and K. von Schuckmann. In situ–based reanalysis of the global ocean temperature and salinity with isas: Variability of the heat content and steric height. *Journal of Climate*, 29:1305–1323, 2016. https://doi.org/10.1175/JCLI-D-15-0028.1.

S. A. Good, M. J. Martin, and N. A. Rayner. En4: quality controlled ocean temperature and salinity profiles and monthly objective analyses with uncertainty estimates. *Journal of Geophysical Research: Oceans*, 118:6704–6716, 2013. https://doi.org/10.1002/2013JC009067.

J. Gourrion, T. Szekely, R. Killick, B. Owens, G. Reverdin, and B. Chapron. Improved statistical method for quality control of hydrographic observations. *Journal of Atmospheric and Oceanic Technology*, 37, 2020. https://doi.org/10.1175/JTECH-D-18-0244.1.

B. Huang, X. Yin, J. A. Carton, L. Chen, G. Graham, P. Hogan, et al. Record high sea surface temperatures in 2023. *Geophysical Research Letters*, 51:e2024GL108369, 2024. https://doi.org/10.1029/2024GL108369.

B. Huang, Chunying Liu Matthew Menne Yuhan Douglas Rao Thomas Smith Russell Vose Xungang Yin, Tim Boyer, and Huai-Min Zhang. Extended reconstructed sea surface temperature, version 6 (ersstv6). part i: An artificial neural network approach. *J. Climate*, 38:1105–1121, 2025. https://doi.org/10.1175/JCLI-D-23-0707.1.

IPCC. Climate Change 2023: Synthesis Report. Contribution of Working Groups I, II and III to the Sixth Assessment Report of the Intergovernmental Panel on Climate Change, 2023. URL https://www.researchgate.net/publication/372768149_Climate_Change_2023_Synthesis_Report_Full_Volume_Contribution_of_Working_Groups_I_II_and_III_to_the_Sixth_Assessment_Report_of_the_Intergovernmental_Panel_on_Climate_Change.

Steven R. Jayne, Dean Roemmich, Nathalie Zilberman, Stephen C. Riser, Kenneth S. Johnson, Gregory C. Johnson, and Stephen R. Piotrowicz. The argo program present and future. *Oceanography*, 30(2):18–28, 2017. https://doi.org/https://doi.org/10.5670/oceanog.2017.213. Special Issue on Autonomous and Lagrangian Platforms and Sensors: Current and Future Directions in Ocean Sampling (June 2017).

Rachel Killick. *EN.4.2.2 Product User Guide*, August 2021. URL https://hadobs.metoffice.com/en4/EN.4.2.2_Product_User_Guide_v1.0.pdf. First EN4 Product User Guide, Version number incremented when changes are made to the documentation for additions or EN4 version updates.

N. Kolodziejczyk, A. Prigent-Mazella, and F. Gaillard. Isas temperature, salinity, dissolved oxygen gridded fields, 2019.

Nicolas Kolodziejczyk, Annaig Prigent-Mazella, and Fabienne Gaillard. Isas temperature, salinity, dissolved oxygen gridded fields, 2023. URL https://doi.org/10.17882/52367.

P.-Y. Le Traon, A. Reppucci, E. Alvarez Fanjul, L. Aouf, A. Behrens, M. Belmonte, A. Bentamy, L. Bertino, V. E. Brando, M. B. Kreiner, M. Benkiran, T. Carval, S. A. Ciliberti, H. Claustre, E. Clementi, G. Coppini, G. Cossarini, M. De Alfonso Alonso-Muñoyerro, A. Delamarche, G. Dibarboure, F. Dinessen, M. Drevillon, Y. Drillet, Y. Faugere, V. Fernández, A. Fleming, M. I. Garcia-Hermosa, M. G. Sotillo, G. Garric, F. Gasparin, C. Giordan, M. Gehlen, M. L. Gregoire, S. Guinehut, M. Hamon, C. Harris, F. Hernandez, J. B. Hinkler, J. Hoyer, J. Karvonen, S. Kay, R. King, T. Lavergne, B. Lemieux-Dudon, L. Lima, C. Mao, M. J. Martin, S. Masina, A. Melet, B. Buongiorno Nardelli, G. Nolan, A. Pascual, J. Pistoia, A. Palazov, J.-F. Piolle, M. I. Pujol, A.-C. Pequignet, E. Peneva, B. Pérez Gómez, L. Petit de la Villeon, N. Pinardi, A. Pisano, S. Pouliquen, R. Reid, E. Remy, R. Santoleri, J. Siddorn, J. She, J. Staneva, A. Stoffelen, M. Tonani, L. Vandenbulcke, K. von Schuckmann, G. Volpe, C. Wettre, and A. Zacharioudaki. From observation to information and users: The copernicus marine service perspective. *Frontiers in Marine Science*, 6:234, 2019. https://doi.org/10.3389/fmars.2019.00234.

Jean-Michel Lellouche, Eric Greiner, Romain Le Brehon-Bretonniere, Gilles Garric, Angélique Melet, Marie Drillet, Clément Bourdallé-Badie, Mathieu Hamon, Olivier Le Galloudec, Charly Regnier, Tony Candela, Charles-Emmanuel Talandier, Florent Testut, Giovanni Ruggiero, Mounir Benkiran, Yann Drévillon, and Pierre-Yves Le Traon. The copernicus global 1/12° oceanic and sea ice glorys12 reanalysis. *Frontiers in Earth Science*, 9:698876, 2021. https://doi.org/10.3389/feart.2021.698876.

S. Levitus, J. I. Antonov, T. P. Boyer, O. K. Baranova, H. E. Garcia, R. A. Locarnini, A. V. Mishonov, J. R. Reagan, D. Seidov, E. S. Yarosh, and M. M. Zweng. World ocean heat content and thermosteric sea level change (0–2000 m) 1955–2010. *Geophysical Research Letters*, 39:L10603, 2012. https://doi.org/10.1029/2012GL051106.

Yuehua Li, John A. Church, Trevor J. McDougall, and Paul M. Barker. Sensitivity of observationally based estimates of ocean heat content and thermal expansion to vertical interpolation schemes. *Geophysical Research Letters*, 49(24):e2022GL101079, 2022. https://doi.org/https://doi.org/10.1029/2022GL101079. URL https://agupubs.onlinelibrary.wiley.com/doi/abs/10.1029/2022GL101079. e2022GL101079 2022GL101079.

Xinfeng Liang, Chao Liu, Rui M. Ponte, and Don P. Chambers. A comparison of the variability and changes in global ocean heat content from multiple objective analysis products during the argo period. *J. Climate*, 34:7875–7895, 2021. https://doi.org/10.1175/JCLI-D-20-0794.1.

Chao Liu, Xinfeng Liang, Rui M. Ponte, and Don P. Chambers. "salty drift" of argo floats affects the gridded ocean salinity products. *Journal of Geophysical Research: Oceans*, 129(9), 2024. https://doi.org/10.1029/2023JC020871. License CC BY-NC 4.0.

J. M. Lyman and G. C. Johnson. Estimating annual global upper-ocean heat content anomalies despite irregular in situ ocean sampling. *J. Clim.*, 21:5629–5641, 2008. https://doi.org/10.1175/2008JCLI2259.1.

B. Meyssignac, T. Boyer, Z. Zhao, M. Z. Hakuba, F. W. Landerer, D. Stammer, A. Köhl, S. Kato, T. L'Ecuyer, M. Ablain, J. P. Abraham, A. Blazquez, A. Cazenave, J. A. Church, R. Cowley, L. Cheng, C. M. Domingues, D. Giglio, V. Gouretski, M. Ishii, G. C. Johnson, R. E. Killick, D. Legler, W. Llovel, J. Lyman, M. D. Palmer, S. Piotrowicz, S. G. Purkey, D. Roemmich, R. Roca, A. Savita, K. von Schuckmann,

S. Speich, G. Stephens, G. Wang, S. E. Wijffels, and N. Zilberman. Measuring global ocean heat content to estimate the earth energy imbalance. *Frontiers in Marine Science*, 6:432, 2019. https://doi.org/10.3389/fmars.2019.00432.

P. P. Niiler. The world ocean surface circulation. In G. Siedler, J. Church, and J. Gould, editors, *Ocean Circulation and Climate*, volume 77 of *International Geophysics Series*, pages 193–204. Academic Press, 2001. URL https://www.sciencedirect.com/science/chapter/bookseries/abs/pii/S0074614201801194.

Y. Pan, A. Minière, K. von Schuckmann, et al. Ocean heat content in 2024. *Nature Reviews Earth & Environment*, 6:249–251, 2025. https://doi.org/10.1038/s43017-025-00655-0. URL https://doi.org/10.1038/s43017-025-00655-0.

James R. Reagan, Tim P. Boyer, Hernán E. García, Ricardo A. Locarnini, Olga K. Baranova, Courtney Bouchard, Scott L. Cross, Alexey V. Mishonov, Christopher R. Paver, Dan Seidov, Zhankun Wang, and Dmitry Dukhovskoy. World ocean atlas 2023, 2024. NOAA National Centers for Environmental Information.

Dean Roemmich, Gregory C. Johnson, Stephen Riser, Russ Davis, John Gilson, W. Brechner Owens, Silvia L. Garzoli, Claudia Schmid, and Mark Ignaszewski. The argo program: Observing the global ocean with profiling floats. *Oceanography*, 22(2):34–43, 2009. Special Issue on the Tenth Anniversary of the National Oceanographic Partnership Program (June 2009).

F. Roquet, C. Guinet, J.-B. Charrassin, D. P. Costa, K. M. Kovacs, C. Lydersen, H. Bornemann, M. N. Bester, M. C. Muelbert, M. A. Hindell, C. R. McMahon, R. Harcourt, L. Boehme, M. A. Fedak, V. Doriot, and B. Picard. MEOP-CTD in-situ data collection: a Southern ocean marine-mammals calibrated sea water temperatures and salinities observations, 2017. URL https://www.seanoe.org/data/00343/45461/#52699. Release 2017-11.

Michela Sammartino, Salvatore Aronica, Rosalia Santoleri, and Bruno Buongiorno Nardelli. Retrieving mediterranean sea surface salinity distribution and interannual trends from multi-sensor satellite and in situ data. *Remote Sensing*, 14(2502), 2022. URL https://www.mdpi.com/2072-4292/14/10/2502.

Wei Shi and Menghua Wang. Monitoring the amazon river plume from satellite observations. *GIScience & Remote Sensing*, 61(1):2416725, 2024. https://doi.org/10.1080/15481603.2024.2416725. URL https://doi.org/10.1080/15481603.2024.2416725.

T. Szekely. *In Situ TAC Objective Analysis Product*, 2024a. URL https://documentation.marine.copernicus.eu/QUID/CMEMS-INS-QUID-013-052.pdf. Contributors: T. Szekely.

T. Szekely. Delayed time mode validation: Minimum / maximum temperature and salinity reference field, 2024b. URL https://archimer.ifremer.fr/doc/00924/103578/.

T. Szekely, J. Gourrion, S. Pouliquen, and G. Reverdin. The cora 5.2 dataset for global in situ temperature and salinity measurements: data description and validation. *Ocean Science*, 15(6):1601–1614, 2019. https://doi.org/10.5194/os-15-1601-2019. URL https://os.copernicus.org/articles/15/1601/2019/.

Tanguy Szekely. Quality information document for in situ TAC products: Global T&S multi-year product (INSITU_GLO_PHY_TS_DISCRETE_MY_013_001). Quality Information Document CMEMS-INS-QUID-013-001, Issue 1.16, Copernicus Marine Service, In Situ Thematic Assembly Centre, April 2025. URL https://documentation.marine.copernicus.eu/QUID/CMEMS-INS-QUID-013-001.pdf. Approved by the Copernicus Marine Service product quality coordination team on 5 November 2025.

L. Tang, H. Zhou, J. Li, P. Wang, X. Su, and Z. Luo. Effect of argo salinity drift since 2016 on the estimation of regional steric sea level change rates. *Remote Sensing*, 16(11):1855, 2024. https://doi.org/10.3390/rs16111855.

C.-C. Teng, L. Bernard, L. LeBlanc, B. Hansen, and R. Crout. Test and evaluation of refreshed tropical atmosphere ocean (tao) buoy system. In *OCEANS 2008 - MTS/IEEE Kobe Techno-Ocean*, pages 1–7, Kobe, Japan, 2008. https://doi.org/10.1109/OCEANSKOBE.2008.4531027.

J. Terhaar, F. A. Burger, L. Vogt, et al. Record sea surface temperature jump in 2023–2024 unlikely but not unexpected. *Nature*, 639:942–946, 2025. https://doi.org/10.1038/s41586-025-08674-z.

H.L. Varona, D. Veleda, M. Silva, M. Cintra, and M. Araujo. Amazon river plume influence on western tropical atlantic dynamic variability. *Dynamics of Atmospheres and Oceans*, 85:1–15, 2019. ISSN 0377-0265. https://doi.org/https://doi.org/10.1016/j.dynatmoce.2018.10.002. URL https://www.sciencedirect.com/science/article/pii/S0377026517300866.

K. von Schuckmann and P.-Y. Le Traon. How well can we derive global ocean indicators from argo data? *Ocean Science*, 7:783–791, 2011. https://doi.org/10.5194/os-7-783-2011.

K. von Schuckmann, A. Minière, F. Gues, F. J. Cuesta-Valero, G. Kirchengast, S. Adusumilli, F. Straneo, M. Ablain, R. P. Allan, P. M. Barker, H. Beltrami, A. Blazquez, T. Boyer, L. Cheng, J. Church, D. Desbruyeres, H. Dolman, C. M. Domingues, A. García-García, D. Giglio, J. E. Gilson, M. Gorfer, L. Haimberger, M. Z. Hakuba, S. Hendricks, S. Hosoda, G. C. Johnson, R. Killick, B. King, N. Kolodziejczyk, A. Korosov, G. Krinner, M. Kuusela, F. W. Landerer, M. Langer, T. Lavergne, I. Lawrence, Y. Li, J. Lyman, F. Marti, B. Marzeion, M. Mayer, A. H. MacDougall, T. McDougall, D. P. Monselesan, J. Nitzbon, I. Otosaka, J. Peng, S. Purkey, D. Roemmich, K. Sato, K. Sato, A. Savita, A. Schweiger, A. Shepherd, S. I. Seneviratne, L. Simons, D. A. Slater, T. Slater, A. K. Steiner, T. Suga, T. Szekely, W. Thiery, M.-L. Timmermans, I. Vanderkelen, S. E. Wjiffels, T. Wu, and M. Zemp. Heat stored in the earth system 1960–2020: where does the energy go? *Earth System Science Data*, 15(4):1675–1709, 2023. https://doi.org/10.5194/essd-15-1675-2023. URL https://essd.copernicus.org/articles/15/1675/2023/.

Karina von Schuckmann, Jean-Baptiste Sallée, D. Chambers, Pierre-Yves Le Traon, C. Cabanes, et al. Monitoring ocean heat content from the current generation of global ocean observing systems. *Ocean Science Discussions*, 10:923–949, 2013. https://doi.org/10.5194/osd-10-923-2013.

H. Wehde, K. von Schuckmann, S. Pouliquen, A. Grouazel, T. Bartolome, J. Tintoré, M. De Alfonso Alonso-Muñoyerro, T. Carval, V. Racapé, and In Situ TAC team. Quality information document for in situ products: Regional multiparameter MYNRT products (INSITU_GLO_PHYBGCWAV_DISCRETE_MYNRT_013_030 to INSITU_NWS_PHYBGCWAV_DISCRETE_MYNRT_013_036). Quality Information Document CMEMS-INS-QUID-013-030-036, Issue 2.5, Copernicus Marine Service, In Situ Thematic Assembly Centre, May 2025. URL https://documentation.marine.copernicus.eu/QUID/CMEMS-INS-QUID-013-030-036.pdf. Approved by the CMEMS product quality coordination team on 6 November 2025.

A. P. Wong, S. E. Wijffels, S. C. Riser, S. Pouliquen, S. Hosoda, D. Roemmich, and et al. Argo data 1999–2019: Two million temperature–salinity profiles and subsurface velocity observations from a global array of profiling floats. *Frontiers in Marine Science*, 7:700, 2020. https://doi.org/10.3389/fmars.2020.00700.

Annie P. S. Wong, John Gilson, and Cécile Cabanes. Argo salinity: bias and uncertainty evaluation. *Earth Syst. Sci. Data*, 15:383–393, 2023. https://doi.org/10.5194/essd-15-383-2023.